Journal of Materials Chemistry A

PAPER

View Article Online
View Journal | View Issue

Cite this: J. Mater. Chem. A, 2017, 5, 4172

Tunable thermodynamic activity of $La_xSr_{1-x}Mn_yAl_{1-y}O_{3-\delta}$ ($0 \leq x \leq 1$, $0 \leq y \leq 1$) perovskites for solar thermochemical fuel synthesis†

M. Ezbiri,[ab] M. Takacs,[a] D. Theiler,[a] R. Michalsky*[a] and A. Steinfeld[a]

Received 3rd August 2016
Accepted 23rd January 2017

DOI: 10.1039/c6ta06644e

rsc.li/materials-a

Nonstoichiometric metal oxides with variable valence are attractive redox materials for thermochemical and electrochemical fuel processing. To guide the design of advanced redox materials for solar-driven splitting of CO_2 and/or H_2O to produce CO and/or H_2 (syngas), we investigate the equilibrium thermodynamics of the $La_xSr_{1-x}Mn_yAl_{1-y}O_{3-\delta}$ perovskite family ($0 \leq x \leq 1$, $0 \leq y \leq 1$) and $La_{0.6}Ca_{0.4}Mn_{0.8}Al_{0.2}O_{3-\delta}$, and compare them to those of CeO_2 as the baseline. Oxygen nonstoichiometry measurements from 1573 to 1773 K and from 0.206 to 180 mbar O_2 show a tunable reduction extent, increasing with increasing Sr content. Maximal nonstoichiometry of 0.32 is established with $La_{0.2}Sr_{0.8}Mn_{0.8}Al_{0.2}O_{3-\delta}$ at 1773 K and 2.37 mbar O_2. As a trend, we find that oxygen capacities are most sensitive to the A-cation composition. Partial molar enthalpy, entropy and Gibbs free energy changes for oxide reduction are extracted from the experimental data using defect models for Mn^{4+}/Mn^{3+} and Mn^{3+}/Mn^{2+} redox couples. We find that perovskites exhibit typically decreasing enthalpy changes with increasing nonstoichiometries. This desirable characteristic is most pronounced by $La_{0.6}Sr_{0.4}Mn_{0.4}Al_{0.6}O_{3-\delta}$, rendering it attractive for CO_2 and H_2O splitting. Generally, perovskites show lower enthalpy and entropy changes than ceria, resulting in more favorable reduction but less favorable oxidation equilibria. The energy penalties due to larger temperature swings and excess oxidants are discussed in particular. Using electronic structure theory, we conclude with a practical methodology estimating thermodynamic activity to rationally design perovskites with variable stoichiometry and valence.

Introduction

Solar fuels can be synthesized *via* electrochemical, photochemical, and thermochemical splitting of H_2O and CO_2.[1–7] The latter approach utilizes the entire spectrum of solar radiation in the form of high-temperature process heat for the production of CO and H_2 (syngas) *via* metal oxide redox cycles.[2,5,8–13] Conceptually, a metal oxide is first reduced endothermically at low partial pressures of O_2 (pO_2) and elevated temperatures using concentrated solar energy. The reduced metal oxide is then re-oxidized exothermically at lower temperatures with CO_2 and H_2O to produce syngas.[14] For this cycle, nonstoichiometric ceria (CeO_2) has become the benchmark redox material due to its favorable oxidation thermodynamics, reaction kinetics, and phase stability.[8,14–18] However, CeO_2 requires high reduction temperatures to reach reasonable oxygen nonstoichiometries, typically above 1673 K, resulting in technically challenging process conditions.[11,19]

Perovskites with $ABO_{3-\delta}$ stoichiometry, where A and B are metal cations in twelve- and six-coordinated interstices, are promising redox materials[3,9,15,19–24] due to their high oxygen vacancy conductivities and the potential to utilize changes in the metal cation composition to control the temperature requirements and the extent of the O_2 evolution reaction. The two-step cycle is represented by:

Perovskite reduction:

$$\frac{1}{\delta_{red}-\delta_{ox}}ABO_{3-\delta_{ox}} \rightarrow \frac{1}{\delta_{red}-\delta_{ox}}ABO_{3-\delta_{red}} + \frac{1}{2}O_2 \quad (1)$$

Perovskite oxidation:

$$\frac{1}{\delta_{red}-\delta_{ox}}ABO_{3-\delta_{red}} + H_2O \rightarrow \frac{1}{\delta_{red}-\delta_{ox}}ABO_{3-\delta_{ox}} + H_2 \quad (2a)$$

$$\frac{1}{\delta_{red}-\delta_{ox}}ABO_{3-\delta_{red}} + CO_2 \rightarrow \frac{1}{\delta_{red}-\delta_{ox}}ABO_{3-\delta_{ox}} + CO \quad (2b)$$

[a]Department of Mechanical and Process Engineering, ETH Zürich, 8092 Zürich, Switzerland. E-mail: michalskyr@ethz.ch

[b]Solar Technology Laboratory, Paul Scherrer Institute, 5232 Villigen-PSI, Switzerland

† Electronic supplementary information (ESI) available: Computational details, comprehensive XRD analyses, oxygen nonstoichiometry measurements and thermodynamic characterization of the perovskites. See DOI: 10.1039/c6ta06644e

We note that the oxygen nonstoichiometry after reduction and oxidation is marked by δ_{red} and δ_{ox}, respectively. The difference in these values is the oxygen exchange capacity, $\Delta\delta = \delta_{red} - \delta_{ox}$, which is equivalent to the specific amount of fuel produced per redox cycle.

While the possibility to establish high oxygen nonstoichiometries at moderate reduction temperatures is well studied for perovskites, the thermochemical activity of these oxygen vacancies in CO_2 and H_2O splitting and the required oxidation conditions are poorly understood. Scheffe *et al.*[15] investigated the redox activity of $La_{0.7}Sr_{0.3}MnO_{3-\delta}$ and $La_{0.6}Sr_{0.4}MnO_{3-\delta}$ predicting their reduction extents to be more than six times larger at 1600 K and two times larger at 1800 K than that of CeO_2, with all materials tested at 10^{-5} bar O_2.[15] Including the metal oxide oxidation, McDaniel *et al.*[19] illustrated that doping $La_{0.6}Sr_{0.4}MnO_{3-\delta}$ with Al resulted in nine and six times greater H_2 and CO yields, relative to CeO_2, when reduced at 1623 K and pO_2 = 0.200 mbar and re-oxidized at 1273 K under 40 vol% H_2O and CO_2, respectively.[19] Recent studies by Cooper *et al.*[23] and Takacs *et al.*[24] confirmed these high reduction extents with Al-doped $La_xSr_{1-x}MnO_{3-\delta}$ and showed how this material characteristic can be even further increased when replacing Sr by Ca. Similarly, Yang *et al.*[3] showed that increasing the Sr content up to $x = 0.4$ in $La_{1-x}Sr_xMnO_{3-\delta}$ increases fuel yields, but decreases fuel production rates when oxidizing at 1073 K with 20 vol% H_2O. In summary, reduction of perovskite redox materials is thermodynamically more favorable than that of CeO_2 at an identical temperature and pO_2, which is, however, at the expense of thermodynamically less favorable perovskite oxidation.

Deml *et al.*[25] reported a computational and experimental investigation of doping in $La_xSr_{1-x}Mn_yAl_{1-y}O_{3-\delta}$ (LSMA), demonstrating the tunability of density functional theory (DFT) calculated oxygen vacancy formation energies for these perovskites. Also, this work reports a correlation between increasing Sr content and an energetically more favorable oxygen vacancy formation, which remains essentially unchanged with changing Mn content. Studies testing perovskites other than LSMA include $La_{1-x}Ca_xMnO_3$, $Ln_{0.5}Sr_{0.5}MnO_3$ and $Ln_{0.5}Ca_{0.5}MnO_3$ (Ln = La, Nd, Sm, Gd, Dy, and Y) where the Y-doped perovskite showed the highest oxygen release, since Y introduces the highest lattice distortion due to large cation size differences.[21,26] Furthermore, $La_xA_{1-x}Mn_yB_{1-y}O_3$ (A = Sr, Ba, Ca, Y; B = Al, Mg),[22] $La_xSr_{1-x}MO_3$ (M = Mn, Co, Fe)[20] and $Ba_xSr_{1-x}(Co,Fe)O_3$ (ref. 20) were shown to reduce more than CeO_2, but also at the expense of oxidation yields. Bork *et al.*[27] investigated $La_{0.6}Sr_{0.4}Cr_{1-x}Co_xO_3$ and showed that Co doping with $x = 0.2$ increased the CO_2 splitting yield 25 fold compared to CeO_2 cycled between oxidation at 1073 K and 1 bar CO_2 and reduction at 1473 K at 10^{-5} bar O_2.

In summary, a fair comparison of oxygen exchange capacities and fuel production rates with perovskite redox materials is currently difficult due to variable reaction conditions and limited data on the perovskite oxidation. Favorable solar fuel production yields with perovskites are obtained for instance with large CO_2 or H_2O oxidant flows during the fuel production step (*cf.* eqn (2a)/(b)) and low pO_2 during the O_2 evolution step, either using a thermogravimetric analyzer (TGA)[20,21,26,27] or an electrically heated furnace and on-line analysis of the gas flows.[19,21] However, such large oxidant concentrations complicate comparisons of fuel yields obtained with materials tested under more realistic conditions relevant to an industrial implementation[3,15,23,24] and would consume larger amounts of energy for gas separations in an industrial setting. Therefore, we measured oxygen nonstoichiometries to accurately compute the fuel yields for various LSMA-type perovskites, and CeO_2 as a reference, at temperatures and pO_2 relevant for thermochemical fuel production processes. We conclude with electronic structure theory computations pinpointing the thermodynamic activity of perovskites with a large range of possible metal cation compositions for renewable syngas production.

Materials and methods

Sample preparation

Perovskite powders were synthesized by a modified Pechini method, using stoichiometric amounts of $La(NO_3)_3 \cdot 6H_2O$ (Sigma Aldrich, 99.999%), $Sr(NO_3)_2$ (Sigma Aldrich, 98%), $Mn(NO_3)_2 \cdot 4H_2O$ (Alfa Aesar, 98%), $Al(NO_3)_3 \cdot 9H_2O$ (Alfa Aesar, 98%), $Ca(NO_3)_2 \cdot 4H_2O$ (Alfa Aesar, 99%), C_2H_6O (Alcosuisse, >96.1 vol%) and $C_6H_8O_7$ (Fluka Chemika, ≥99.5%). The ratio of metal cations to citric acid was 2 : 3. The solid products were ground using a mortar and pestle and calcined at 1273 K in air for 5 h with heating and cooling at 5 K min^{-1}. The powders obtained were cold-pressed uniaxially into pellets (5 metric tons, 8 mm in diameter) and sintered in air at 1773 K for 24 h with heating and cooling at 2.5 K min^{-1}.

Solid-state analysis

X-ray diffraction (XRD) was performed in the Bragg Brentano geometry using Cu Kα radiation (20–80° 2θ, 0.01° min^{-1} scan rate, 45 kV/20 mA output, PANalytical/X'Pert MPD/DY636, Philips). Basic structural data were obtained by multiphase analysis (Jana2006). Scanning electron microscopy (SEM; 3 kV accelerating voltage, SmartSEM, Supra 55VP) was used to analyze the morphology, excluding conceivable phase segregation for all samples.

Thermal analysis

The mass change of the samples was measured as a function of temperature and pO_2 using a TGA (Setaram Setsys Evolution). Perovskite pellets (129 mg to 208 mg) were suspended at the scale (±0.02 μg accuracy) with a platinum hook. The materials were exposed to a constant flow rate of 200 mL min^{-1} (volumes are given as measured at 298 K and 1 bar). The variable pO_2 was adjusted *via* mixing Ar (Messer, Argon 4.6) with O_2/Ar mixtures (Messer, O_2 5.0 in Ar 5.0) using electronic mass flow controllers (Brooks, Model 5850TR, accuracy ±1%). Temperature was varied between 1373 K and 1773 K and pO_2 between 0.206 mbar and 180 mbar. The gas composition was monitored at the TGA outlet with a mass spectrometer (Pfeiffer Vacuum, Omnistar GSD 320). To correct for buoyancy, blank runs were performed with sintered Al_2O_3 pellets with sample dimensions.

Oxygen defect modelling

A defect model[28] based on the oxygen-deficient region of doped $LaMnO_{3-\delta}$ was used to describe the chemical equilibria of the perovskites. Upon doping $LaMnO_3$ (containing La^{3+} denoted as $La^{\times}$ and Mn^{3+} denoted as $Mn^{\times}$) with a divalent metal cation (*e.g.* Sr^{2+} denoted as Sr'), the oxidation state of some Mn cations changes from trivalent to tetravalent (*i.e.* Mn^{4+} denoted as $Mn^{\bullet}$), such that doped $LaMnO_3$ is written as $La^{\times}_{1-x}Sr'_xMn^{\times}_{1-x}Mn^{\bullet}_xO_3$ in Kröger–Vink notation.[29] Therefore, the defect structure of doped and undoped $LaMnO_{3-\delta}$ was computed assuming two simultaneous Mn^{4+}/Mn^{3+} and Mn^{3+}/Mn^{2+} redox couples.[24,28] We note that this defect model does not consider formation of defect clusters such as of oxygen vacancies or neighboring B-site cations[30,31] since such clusters are expected to form only at pO_2 levels below those investigated here.[32]

During reduction of the doped perovskite, some $Mn^{\bullet}_{Mn}$ (Mn^{4+} in Mn^{3+} sites) reduces to $Mn^{\times}_{Mn}$ (Mn^{3+} in Mn^{3+} sites) while lattice oxygen ($O^{\times}_O$) is released as molecular O_2 forming doubly ionized oxygen vacancies ($V^{\bullet\bullet}_O$) (*cf.* eqn (3)).[15,23,24,28,32–36]

$$O^{\times}_O + 2Mn^{\bullet}_{Mn} \leftrightarrow V^{\bullet\bullet}_O + 2Mn^{\times}_{Mn} + \frac{1}{2}O_2(g) \quad (3)$$

The equilibrium constant for this point defect reaction (K_1) is given with eqn (4),[23,24,34,35] assuming activity coefficients equal to 1 and standard pressure $p^{\circ} = 1$ bar:

$$K_1 = \frac{\left[V^{\bullet\bullet}_O\right]\left[Mn^{\times}_{Mn}\right]^2}{\left[O^{\times}_O\right]\left[Mn^{\bullet}_{Mn}\right]^2}\left(\frac{pO_2}{p^{\circ}}\right)^{1/2} \quad (4)$$

Square brackets denote concentrations taken as sublattice site fractions. $Mn^{\times}_{Mn}$ can further disproportionate into Mn'_{Mn} (Mn^{2+} in Mn^{3+} sites) and $Mn^{\bullet}_{Mn}$ (*cf.* eqn (5)).

$$2Mn^{\times}_{Mn} \leftrightarrow Mn^{\bullet}_{Mn} + Mn'_{Mn} \quad (5)$$

Combining eqn (3) and (5), the disproportionation reaction can be rewritten as[24]

$$O^{\times}_O + Mn^{\bullet}_{Mn} \leftrightarrow V^{\bullet\bullet}_O + Mn'_{Mn} + \frac{1}{2}O_2(g) \quad (6)$$

resulting in a second equilibrium constant (K_2):

$$K_2 = \frac{\left[V^{\bullet\bullet}_O\right]\left[Mn'_{Mn}\right]}{\left[O^{\times}_O\right]\left[Mn^{\bullet}_{Mn}\right]}\left(\frac{pO_2}{p^{\circ}}\right)^{1/2} \quad (7)$$

Based on the site balances for manganese and oxygen and charge neutrality (*cf.* eqn (8) and (9), respectively), K_1 and K_2 can be related to eqn (10).[24]

$$\begin{aligned} n_{Mn^{\bullet}_{Mn}} + n_{Mn^{\times}_{Mn}} + n_{Mn'_{Mn}} &= 1 - y \\ n_{O^{\times}_O} + n_{V^{\bullet\bullet}_O} &= 3 \end{aligned} \quad (8)$$

$$2n_{V^{\bullet\bullet}_O} + n_{Mn^{\bullet}_{Mn}} = x + n_{Mn'_{Mn}} \quad (9)$$

$$\underbrace{\frac{\delta^{1/2}(x+y-2\delta-1)(pO_2/p^{\circ})^{1/4}}{(x-2\delta)(3-\delta)^{1/2}}}_{Y} = \underbrace{\frac{(3-\delta)^{1/2}(2\delta-x+y-1)}{\delta^{1/2}(x-2\delta)(pO_2/p^{\circ})^{1/4}}}_{X} * K_2 - K_1{}^{1/2} \quad (10)$$

Using eqn (10), K_1 and K_2 can then be extracted by plotting X *vs.* Y, both derived from the experimental results, and with $-K_1{}^{1/2}$ representing the y-intercept and K_2 the slope of the linear fit. Individual and fitted equilibrium constants K_1 and K_2 as a function of $1000/T$ are shown in Fig. S4.† The fitting parameters used for Fig. S4† are the enthalpy Δh°_i and entropy Δs°_i of the single defect reactions ($i = 1$ for eqn (3) and $i = 2$ for eqn (6)):

$$-\ln(K_i) = \frac{\Delta h^{\circ}_i}{RT} - \frac{\Delta s^{\circ}_i}{R}, \quad i = 1,\ 2 \quad (11)$$

Once K_1 and K_2 are determined, eqn (10) can be solved to obtain δ as a function of pO_2. In this work, the equilibrium constants K_1 and K_2 were used to fit the measured oxygen nonstoichiometry data of LSMA and LCMA perovskites to model to oxygen nonstoichiometry as a function of temperature and pO_2. Further details of this procedure are given by Takacs *et al.*[24]

Electronic structure calculations

All DFT calculations were performed using the grid-based projector-augmented wave (GPAW) code.[37,38] Atomic configurations were handled in the atomic simulation environment (ASE),[39] with exchange–correlation interactions treated by the revised Perdew–Burke–Ernzerhof (RPBE) functional.[40] The atomic geometries were optimized employing the linesearch Broyden–Fletcher–Goldfarb–Shanno (BFGS) algorithm until the maximum force was less than 0.05 eV $Å^{-1}$. Convergence was achieved using a Fermi–Dirac smearing of 0.1 eV. The results were extrapolated to 0 K. Similar to previous studies,[41,42] all DFT calculations reported here use the generalized gradient approximation (GGA) without a Hubbard U correction, since we have demonstrated previously that this addition does not improve calculations of the surface activity with the employed models.[43,44] $AA'BB'O_3$ perovskites were modeled with $A_4B_4O_{12}$ models containing a cubic ABO_3 unit cell repeated once in x- and z-directions, with La and Sr at the twelve-coordinated A-site interstices, and Mn and Al at the six-coordinated B-site interstices. All atoms of the bulk models were allowed to optimize their positions (relax). Three compositions with different metal ratios (*i.e.* $La_{0.25}Sr_{0.75}Mn_{0.75}Al_{0.25}O_{3-\delta}$, $La_{0.75}Sr_{0.25}Mn_{0.25}Al_{0.75}O_{3-\delta}$ and $La_{0.75}Sr_{0.25}Mn_{0.75}Al_{0.25}O_{3-\delta}$) were modeled by replacing one atom of the perovskite model at the A-site or B-site, respectively. The Brillouin zone of these bulk models having periodic boundary conditions in all directions was sampled with $4 \times 4 \times 4$ k-points. All compositions contained Mn and were therefore modeled using spin-polarized calculations. The computed lattice constants are within ±1.18–2.79% of experimental values and are given along with the magnetic moments in the ESI.† The perovskite surfaces were modeled using the (010) facet with AO-termination, that is geometrically symmetric

with the (001) and (100) facet dependent on composition, that is the thermodynamically most stable surface.[44] The surface models contained the same number of atoms as the bulk models, *i.e.*, had $A_4B_4O_{12}$ stoichiometry, of which the upper $A_2B_2O_6$ layer parallel to the surface was allowed to relax, while the lower layer was constrained to the bulk geometry. All surface structures were periodically repeated parallel to the surface, used 10 Å of vacuum perpendicular to the surface, and employed a *k*-point sampling of 4 × 4 × 1. To model reduced perovskite surfaces, one sixth of the stoichiometric lattice oxygen was removed from the upper surface layer, *i.e.*, $A_4B_4O_{11}$ models representing $\delta = 0.25$.

The Gibbs free energy change of oxygen vacancy formation ($\Delta G_V[O]$) was computed with:[44]

$$\Delta G_V[O] = G_V - (G_S - G_O^r) \quad (12)$$

with G_V and G_S being the Gibbs free energies of formation of the perovskite surfaces with and without oxygen vacancies, respectively, while G_O^r is the reference free energy of the liberated lattice oxygen taken as the energy difference of stable H_2O and H_2 in the gas phase. Negative free energies correspond to exergonic reactions.

The design principle for metal oxide redox materials that we introduce in this work employs the standard enthalpy change of the metal oxide bulk reduction at 298 K and 1 bar total pressure $\left(-\Delta\bar{h}_O^{\circ *}\right)$ as a descriptor for the standard partial molar Gibbs free energy change of the metal oxide bulk reduction and oxidation $\left(\Delta\bar{g}_O^{\circ *}\text{ and }-\Delta\bar{g}_O^{\circ}\right)$, respectively. For a limited number of mostly stoichiometric metal oxides, $\Delta\bar{h}_O^{\circ *}$ can be computed from tabulated thermochemical data.[45] To estimate $\Delta\bar{h}_O^{\circ *}$ for complex metal oxides where such data are not available, we employed previously reported scaling relationships between $\Delta\bar{h}_O^{\circ *}$ and $\Delta G_V[O]$.[44] This circumvents the need for computationally demanding phonon calculations for estimating thermochemical properties of solid materials. The linear scaling relationship utilized in this work is:

$$\Delta G_v[O] = 4.49069 \times 10^{-3}\,\frac{\text{eV}}{\text{kJ mol}_O^{-1}}\,\Delta\bar{h}_O^{\circ *} - 8.16401 \times 10^{-1}\ \text{eV} \quad (13)$$

Thermodynamic properties computed with this scaling relationship are defined per mole of monoatomic oxygen. Details on how the DFT-computed electronic energies were converted into Gibbs free energies at different temperatures and pO_2, the reference energies, and details on the scaling relationship[44] are given in the ESI.†

Results and discussion

Materials characterization

The structural data obtained by multiphase Rietveld analysis of the perovskites are given in Table 1. Lattice distortions, such as the tilting of the anion octahedra, are common in perovskites, causing them to adopt crystal structures other than ideally cubic.[46,47] The investigated Sr doped perovskites all crystallized in the rhombohedral $R\bar{3}c$ phase while LCMA6482 adopted the orthorhombic *Pnma* structure (Table 1), which is in agreement with previously published data.[19,48] The corresponding XRD patterns of the LSMA and LCMA compounds are shown in the ESI.† As opposed to $La_xSr_{1-x}Co_yM_{1-y}O_{3-\delta}$ (M = Mn, Fe),[49] decreasing the molar dopant concentration of La (x_{La}) such as in LSMA2882, did not result in a cubic structure. All perovskites were considered single-phase since the detected impurities were less than 3%, presumably originating from phase segregations into lower-symmetry metal oxides (*i.e.*, $LaMnO_3$, Mn_3O_4, Mn_2O_3, MnO_2, and La_2O_3) and $SrCO_3$. As expected from the size of the ionic radii, lattice parameters increased with increasing x_{La} and y_{Mn}, with LSMA6482 having the largest cell volume of 341.2 Å^3 and LSMA6446 the smallest with 329.6 Å^3.

Table 1 Structural properties calculated from Rietveld analysis of XRD patterns for LSMA and LCMA perovskites

Perovskite	Space group	wt% perovskite	Cell volume (Å^3)
LSMA2882	$R\bar{3}c$ (167)[50]	97.8	331.2
LSMA4682	$R\bar{3}c$ (167)[50]	98.6	337.0
LSMA6482	$R\bar{3}c$ (167)[50]	97.0	341.2
LSMA6446	$R\bar{3}c$ (167)[50]	97.8	329.6
LSMA4664	$R\bar{3}c$ (167)[50]	99.2	333.3
LCMA6482	*Pnma* (62)[51]	97.8	223.2

Oxygen nonstoichiometry measurements

Fig. 1 shows the dynamic oxygen nonstoichiometry measurements of LSMA6482, LCMA6482, LSMA6446, LSMA4664, LSMA4682 and LSMA2882 from 1573 K to 1773 K and from 2.37 mbar O_2 to 45.0 mbar O_2. Mass equilibrium is reached at each temperature and pO_2. The experimental runs at lower (0.206

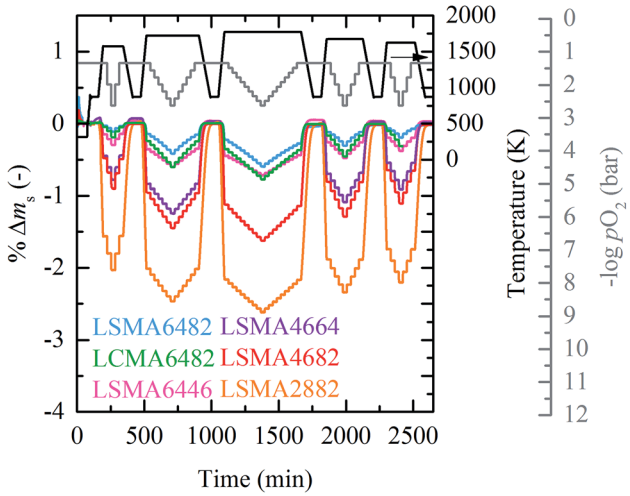

Fig. 1 Percent weight change *vs.* time at 1573 K to 1773 K and 2.37 mbar O_2 to 45.0 mbar O_2 for LSMA6482, LCMA6482, LSMA6446, LSMA4664, LSMA4682 and LSMA2882.

mbar O_2 to 0.901 mbar O_2, *cf.* Fig. S2) and higher (9.48 mbar O_2 to 180 mbar O_2, *cf.* Fig. S3) pO_2 ranges are given in the ESI.† Each experiment consisted of varying pO_2 for oxidation and reduction at different set point temperatures, following the procedure of Takacs *et al.*[24]

Stabilization steps at 873 K were used as reference weight for extracting oxygen nonstoichiometry. LSMA4664 was not measured at 1773 K due to likely phase changes at this temperature. The experiment of LCMA6482 was stopped after 2426 min.

Oxygen nonstoichiometries can be calculated from the data shown in Fig. 1 with:

$$\delta = \Delta m_s \frac{M_s}{M_O} \quad (14)$$

where Δm_s is the relative weight loss at equilibrium, and M_s and M_O are the molar mass of the sample and of monoatomic oxygen, respectively. Δm_s of the reduction and oxidation runs is taken relative to the mass at 873 K, before heating to the set point temperatures and after cooling from the set point temperatures, respectively.

As expected, decreasing pO_2 and increasing temperature resulted in an increase in oxygen nonstoichiometry for all investigated compounds. As seen from Fig. 1, LSMA2882 exhibits the largest reduction extents, while the oxygen nonstoichiometry decreases in the order highest for LSMA4682, LSMA4664, LSMA6446, and LCMA6482, to lowest for LSMA6482. The oxygen nonstoichiometries are shown in Fig. 2 in the form $3-\delta$ and as a function of pO_2 for LSMA6446, LSMA6482 and LSMA2882 from 1573 K to 1773 K. The corresponding plots for LSMA4664, LSMA4682 and LCMA6482 are given in the ESI.† Symbols indicate measured $3-\delta$ obtained by TGA shown in Fig. 1. We assume ideal stoichiometry for all perovskites in the initial oxidized state ($\delta_i = 0$). Attempting to measure the actual stoichiometry of these perovskites was unsuccessful. This is due to their complex quaternary composition, as compared to our previous stoichiometric analysis of binary perovskites.[43] These additional measurements and a sensitivity analysis for our thermochemical calculations to the assumption $\delta_i = 0$ are given in the ESI.†

To show that the oxidation state is not changing with an increase in pO_2, we exposed LSMA2882 for 2 h at 873 K to 0.2 bar O_2. Since this oxidation experiment did not change the mass of the perovskite sample, the oxidation state can be assumed to be relatively pO_2 independent around the reference state. Thus, the actual initial oxygen nonstoichiometry of the studied quaternary perovskites is near the assumed $\delta_i = 0$, within the uncertainty of the employed TGA, which is further supported by Mizusaki *et al.*[33] who investigated the defect structure of La_x-$Sr_{1-x}MnO_{3-\delta}$ perovskites. While the modeling uses $\Delta\delta = \delta - \delta_i$ as input, given $\delta_i = 0$ the text speaks of δ for simplicity.

The values of δ were calculated using pO_2 in the range 10^{-5} to 1 bar based on the computed defect equilibrium constants K_1 and K_2, shown with solid black lines and the dashed colored lines in Fig. 2.

Error bars correspond to mass deviations from zero at the stabilization steps of 873 K (Δm_s of perovskites shown in Fig. 1). All perovskites investigated are described well by the simultaneous redox couples Mn^{4+}/Mn^{3+} and Mn^{3+}/Mn^{2+}, as shown in Fig. 2. Especially for LSMA2882, Fig. 2 shows that deviations between both fits increase with decreasing pO_2, which can be understood due to a mismatch between individual data points and fits of the equilibrium constants. The corresponding plots of LSMA4664, LSMA4682 and LCMA6482 are given in Fig. S5 in the ESI.†

Oxygen defect modelling

Defect models were used to extract oxygen nonstoichiometry at $pO_2 = 10^{-3}$ bar for all studied perovskites, including LSMA6464,[24] and LCMA6464 (ref. 24) as well as CeO_2 (ref. 52) analyzed by Takacs *et al.*[24,52] Table 2 gives the numerical fit values of the defect constants, and Fig. 3 shows the computed oxygen nonstoichiometries. Oxygen nonstoichiometry values of

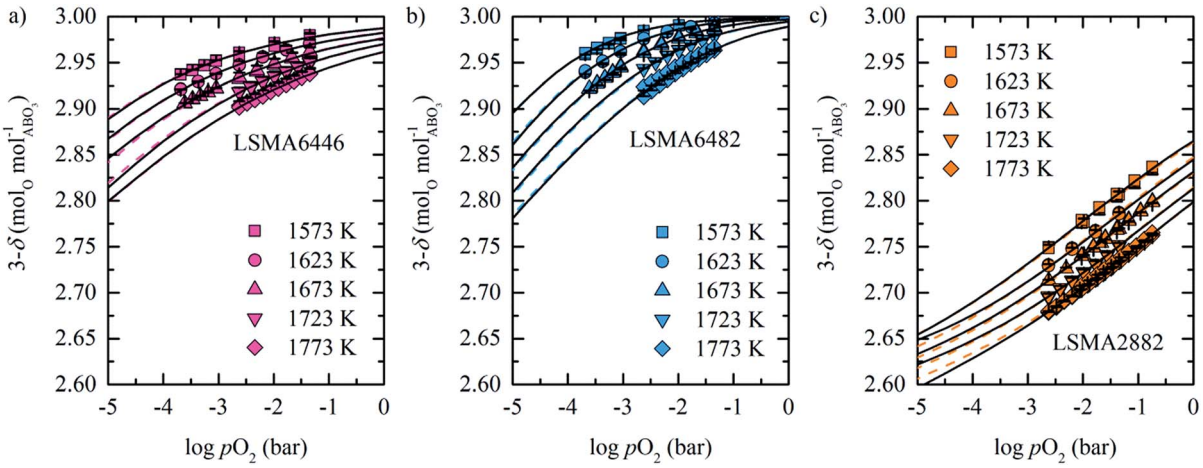

Fig. 2 Measured oxygen nonstoichiometry (symbols) of (a) LSMA6446, (b) LSMA6482 and (c) LSMA2882 as a function of pO_2 for 1573 K to 1773 K. Colored dashed and black solid lines are calculated with defect models, where black solid lines use the individual defect equilibrium constants and colored dashed lines use the inverse temperature dependence of ln K_1 and ln K_2, as shown with lines in Fig. S4.† Error bars correspond to mass deviations from zero at the stabilization steps of 873 K.

Table 2 Linear fitting parameters Δh_i° and Δs_i° of the two defect reactions of ln K_i as a function of 1000/T (*cf.* eqn (11)) of LSMA2882, LSMA6482, LSMA4682, LSMA4664, LSMA6446 and LCMA6482

Defect reaction	Linear fitting parameter	LSMA2882	LSMA6482	LSMA4682	LSMA4664	LSMA6446	LCMA6482
Eqn (3) (K_1)	Δh_1° (kJ mol^{-1})	202.18	494.53	256.05	309.81	442.96	318.44
	Δs_1° (J mol^{-1} K^{-1})	92.23	229.55	111.97	127.77	186.69	133.79
Eqn (6) (K_2)	Δh_2° (kJ mol^{-1})	264.30	370.91	319.12	181.28	222.80	227.07
	Δs_2° (J mol^{-1} K^{-1})	83.33	144.91	118.90	36.79	56.13	63.71

all perovskites far exceed those of CeO_2. As also shown in Fig. 1 and 2, Ca-doped *vs.* Sr-doped compositions have higher reduction extents. This agrees with previous work[24,26] and has been attributed to the smaller ionic radii of Ca^{2+} compared to Sr^{2+}. Furthermore, increasing x_{Sr} results in increasing reduction extents,[20,23,25,26,49,53] which can be attributed to the correlation between the O 2p band center and the free energy change of the oxygen vacancy formation (ΔG_V[O]) in perovskites without a band gap.[25] This is analogous to observations for the oxygen reduction[54] and oxygen evolution reactions[55] in catalysis, namely, when Sr^{2+} occupies La^{3+} sites, electron holes (acceptors) are created. This causes the Fermi energy to decrease into the valence band. Holes can now accept O 2p electrons that are no longer fully bound to the lattice.[25] Analogously, increasing y_{Mn} with constant x_{Sr} does not result in a noticeable shift of ΔG_V[O] since the constant number of holes implies an approximately constant number of unoccupied Mn-bound lattice oxygen.[25] Hence, the temperature differences at which perovskites with changing Mn/Al ratio and constant La/Sr ratio reach a given δ are smaller compared to those obtained for materials with a variable La/Sr ratio and a constant Mn/Al ratio. In particular, LSMA2882, LSMA4682 and LSMA4664 reach $\delta = 0.04$ at 800, 470, and 490 K lower than the temperatures required by CeO_2 to reach the same oxygen nonstoichiometry, respectively. Compositions with a La/Sr ratio of 0.6 : 0.4 reach $\delta = 0.04$ at approximately 200 to 300 K lower, as compared to CeO_2. The same trend is observed for the two Ca-doped compositions, LCMA6464 (ref. 24) and LCMA6482, which reach $\delta = 0.04$ at 260 and 300 K lower than the temperatures required by CeO_2.

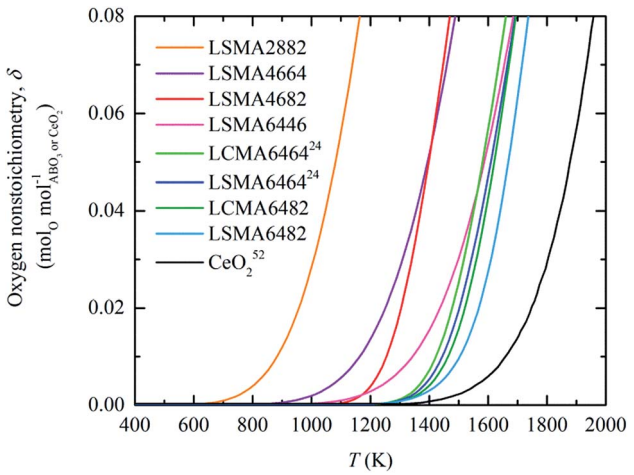

Fig. 3 Oxygen nonstoichiometry of LSMA6446, LSMA4664, LSMA4682, LSMA6482, LSMA2882, LCMA6482, LSMA6464,[24] LCMA6464 (ref. 24) and CeO_2 (ref. 52) as a function of temperature at 10^{-3} bar.

Enthalpy and entropy trends of oxygen nonstoichiometries

In this section, major thermodynamic properties that are useful for comparison and rational design of perovskite redox materials, namely $\Delta\bar{h}_O^\circ$, $\Delta\bar{s}_O^\circ$ and $\Delta\bar{g}_O^\circ$ (all given per mol of oxygen vacancies created in the perovskite lattice), are extracted from the experimental data using the defect models described above and assuming unity activity for all solids and ideal O_2 gas.[3,23,24] Thermodynamic equilibrium for reduction and oxidation with CO_2 is defined according to eqn (15) and (16), respectively:

$$\Delta\bar{g}_O^\circ(\delta, T) = -\frac{1}{2} RT \ln(pO_2/p^\circ) \quad (15)$$

$$\begin{aligned}\Delta\bar{g}_O^\circ(\delta, T) &= RT \ln\left(\frac{K_s(T) pCO_2}{pCO}\right) \\ &= RT \ln(K_s(T)) + RT \ln\left(\frac{pCO_2}{pCO}\right) \\ &= \Delta G_r^\circ + RT \ln\left(\frac{pCO_2}{pCO}\right)\end{aligned} \quad (16)$$

where p° is the standard pressure at 1 bar, K_s is the chemical equilibrium constant of CO_2 dissociation ($CO_2 = CO + 0.5O_2$), ΔG_r° is the standard Gibbs free energy change of CO_2 dissociation and pCO_2 and pCO are the partial pressures of CO_2 and CO.

$\Delta\bar{g}_O^\circ$ can be obtained from $\Delta\bar{h}_O^\circ$ and $\Delta\bar{s}_O^\circ$:

$$\Delta\bar{g}_O^\circ(\delta, T) = \Delta\bar{h}_O^\circ(\delta) - T\Delta\bar{s}_O^\circ(\delta) \quad (17)$$

Eqn (15) and (17) can be rewritten as a linear function with $2\Delta\bar{h}_O^\circ/R$ and $-2\Delta\bar{s}_O^\circ/R$ as the slope and intercept, respectively (*cf.* eqn (18)):

$$-\ln(pO_2/p^\circ) = \frac{2\Delta\bar{h}_O^\circ(\delta)}{RT} - \frac{2\Delta\bar{s}_O^\circ(\delta)}{R}\bigg|_{\delta=\text{const.}} \quad (18)$$

The corresponding plots of $-\ln(pO_2/p^\circ)$ *vs.* $1/T$ are given in Fig. S6.† The good linear fit of the data ($R^2 > 0.98$) confirms temperature independence of $\Delta\bar{h}_O^\circ$ and $\Delta\bar{s}_O^\circ$ for all perovskites under the investigated conditions. Fig. 4 shows $\Delta\bar{h}_O^\circ$ and $\Delta\bar{s}_O^\circ$ as a function of δ for LSMA6446, LSMA6464 and LSMA6482 (*cf.* Fig. 4a and c) and LSMA6482, LSMA4682 and LSMA2882 (*cf.*

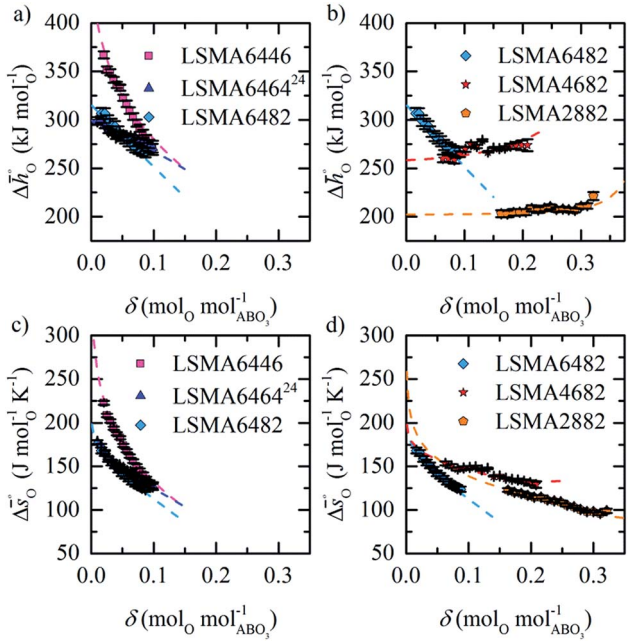

Fig. 4 Standard partial molar enthalpy change $\Delta\bar{h}^\circ_O$ as a function of δ for (a) LSMA6446, LSMA6464 (ref. 24) and LSMA6482 and (b) LSMA6482, LSMA4682 and LSMA2882. Standard partial molar entropy change $\Delta\bar{s}^\circ_O$ as a function of δ for (c) LSMA6446, LSMA6464 (ref. 24) and LSMA6482 and (d) LSMA6482, LSMA4682 and LSMA2882. Symbols are based on measured δ values, shown by the black solid lines, while dashed lines are based on modeled δ values, computed from the values shown with colored dashed lines in Fig. 2 and S7.† Data for LSMA6464 were extracted from the publication by Takacs *et al.*[24]

Fig. 4b and d), displaying LSMA compositions with the same A-, but varying B-cation ratios and the same B-, but varying A-cation ratios, respectively. The corresponding data of LSMA4664 and LCMA6482 are given in Fig. S7† (along with data for LSMA6464,[24] LSMA4682 and LCMA6464 (ref. 24) for comparison). Symbols correspond to the measured δ values shown by the black solid lines, while the dashed lines correspond to the modeled δ values computed from the colored dashed lines of Fig. 2 and S5.† Error bars are $\pm 2\sigma$ confidence intervals of the slope and intercept of $-\ln(pO_2/p^\circ)$ *versus* $1/T$ (*cf.* Fig. S6†) for $\Delta\bar{h}^\circ_O$ and $\Delta\bar{s}^\circ_O$, respectively. Fig. 4 shows a good agreement between measured and modeled $\Delta\bar{h}^\circ_O$ and $\Delta\bar{s}^\circ_O$ values.

Generally, all perovskites show $\Delta\bar{h}^\circ_O$ values lower than those of CeO_2,[52] reflecting their higher reduction extents (*cf.* Fig. 3). For example, at $\delta = 0.1$, $\Delta\bar{h}^\circ_O$ of the perovskites is about 110 to 190 kJ mol$_O^{-1}$ lower when compared to the values for CeO_2.[52] At lower oxygen nonstoichiometry enthalpy changes are more sensitive, such that at $\delta = 0.01\Delta\bar{h}^\circ_O$ is about 70 to 270 kJ mol$_O^{-1}$ lower than the values for CeO_2.[52] Interestingly, $\Delta\bar{h}^\circ_O$ decreases for all compositions with increasing δ (*cf.* Fig. 4a and b) except for LSMA2882 and LSMA4682 (*cf.* Fig. 4b). Increasing enthalpies with increasing oxygen nonstoichiometry had been reported previously for LSM40,[23,24] LCM40,[23,24] and various LSCM[49] ($La_xSr_{1-x}Co_yMn_{1-y}O_{3-\delta}$) and LSCF[49] ($La_xSr_{1-x}Co_yFe_{1-y}O_{3-\delta}$) compositions. The LSCM[49] and LSCF[49] perovskites show generally stronger exergonic and stronger endergonic values at low and high oxygen nonstoichiometries, respectively, than the LSMA and LCMA compositions presented here. The uniquely steep decrease in the enthalpic behavior of LSMA6446 with decreasing oxygen nonstoichiometry stands out (*cf.* Fig. 4a) and will be rationalized in the following.

Regarding the entropic contributions to perovskite reduction, we observe that the perovskites have generally lower $\Delta\bar{s}^\circ_O$ values as compared to CeO_2.[52] For example, at $\delta = 0.1\Delta\bar{s}^\circ_O$ of all the investigated perovskites is between 10 and 40 J mol$_O^{-1}$ K^{-1} lower than those of CeO_2,[52] while at $\delta = 0.01\Delta\bar{s}^\circ_O$ is up to 90 J mol$_O^{-1}$ K^{-1} lower compared to the values for CeO_2.[52] Generally, absolute values for $\Delta\bar{s}^\circ_O$ are decreasing from LSMA6446, over LSMA4664, LSMA2882, LCMA6464,[24] LSMA4682, LSMA6464,[24] and LSMA6482 to lowest for LCMA6482, if $\delta < 0.05$ (*cf.* Fig. 4c, d, S7c and d†). From here we suggest that the larger reduction extent of LSMA6446, relative to LSMA6482 (*cf.* Fig. 1), is due to its larger $\Delta\bar{s}^\circ_O$ values, since $\Delta\bar{h}^\circ_O$ is larger for LSMA6446 than for LSMA6482.

Thermodynamic activity of nonstoichiometric perovskites

Fig. 5 shows $\Delta\bar{g}^\circ_O$ as a function of T, as calculated from $\Delta\bar{h}^\circ_O$ and $\Delta\bar{s}^\circ_O$ (dashed lines in Fig. 4) using eqn (17). $\Delta\bar{g}^\circ_O$ was calculated at $\delta = 0.01$ and from 400 K to 1600 K relevant for the equilibrium after oxidation, as well as at $\delta = 0.1$ and from 1200 K to 2400 K relevant for reduction, for LSMA6446, LSMA6464,[24] LSMA6482, LSMA4682 and LSMA2882, along with CeO_2 (ref. 52) as the reference material. While Fig. 5a shows $\Delta\bar{g}^\circ_O$ of compounds with a constant A-cation ratio and varying B-cation ratios (LSMA6446, LSMA6464,[24] and LSMA6482), Fig. 5b shows perovskites with a constant B-cation ratio and varying A-cation ratios (LSMA6482, LSMA4682, and LSMA2882). $\Delta\bar{g}^\circ_O$ of LSMA4664 and LCMA6482 (along with CeO_2,[52] LSMA6464,[24] LSMA4682 and LCMA6464 (ref. 24) for comparison) is shown in Fig. S8.† Solid grey lines represent the right hand side of eqn (15): $\Delta\bar{g}^\circ_O(\delta, T) = -\frac{1}{2}RT\ln(pO_2/p^\circ)$ with $pO_2 = 10^{-3}$ bar and dashed grey lines represent the right hand side of eqn (16): $\Delta_r G^\circ_{CO_2} = \Delta G^\circ_r + RT\ln\left(\frac{pCO_2}{pCO}\right)$ for $pCO/pCO_2 = 0.01$ where ΔG°_r is the Gibbs free energy change of CO oxidation computed from NIST-JANAF tables.[56] $pO_2 = 10^{-3}$ bar and $pCO/pCO_2 = 0.01$ (equal to 1% CO in CO_2) were chosen as realistic conditions of the reduction and oxidation steps in solar-driven syngas production cycles, respectively.[8] A certain final concentration of CO in CO_2 is usually taken in real reactor systems to avoid low CO_2 conversions.[8] Oxidation to $\delta = 0.01$ is thermodynamically favorable at the temperature at which $-\Delta\bar{g}^\circ_O(\delta, T) = -\Delta_r G^\circ_{CO_2}$. Similarly, reduction to $\delta = 0.1$ is favorable at the temperature at which the equality $\Delta\bar{g}^\circ_O(\delta, T) = -\frac{1}{2}RT\ln(pO_2/p^\circ)$ holds.

From Fig. 5 we conclude that at $pO_2 = 10^{-3}$ bar and $pCO/pCO_2 = 0.01$, CeO_2 has the most favorable oxidation thermodynamics and the least favorable reduction thermodynamics compared to the investigated perovskites (*cf.* Fig. 5a and b). Both oxidation to $\delta = 0.01$ and reduction to $\delta = 0.1$ of CeO_2 are favorable at much higher temperatures. Furthermore, Fig. 5

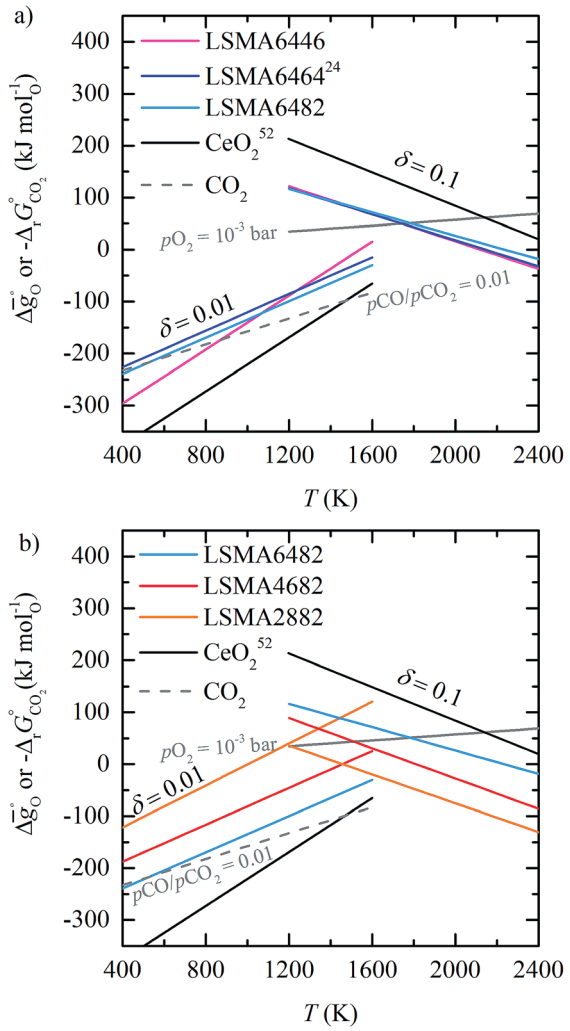

Fig. 5 Standard partial molar Gibbs free energy change $\Delta\bar{g}^{\circ}_{O}$ as a function of T for (a) LSMA6446, LSMA6464,[24] LSMA6482 and CeO_2;[52] and (b) LSMA6482, LSMA4682, LSMA2882 and CeO_2,[52] for $\delta = 0.10$, relevant for metal oxide reduction, and $\delta = 0.01$, relevant for metal oxide oxidation. The dashed grey line represents the Gibbs free energy change of CO oxidation ($CO + 0.5O_2 = CO_2$), $-\Delta_r G^{\circ}_{CO_2}$ in 1% CO in CO_2 ($pCO/pCO_2 = 0.01$). The metal oxide reduction is at equilibrium in $pO_2 = 10^{-3}$ bar at $\delta = 0.10$ and at temperatures at which eqn (15) holds (grey solid line). The metal oxide oxidation with CO_2 to $\delta = 0.01$ at $pCO/pCO_2 = 0.01$ is thermodynamically favorable at temperatures where $-\Delta\bar{g}^{\circ}_{O} = -\Delta_r G^{\circ}_{CO_2}$.

indicates that CeO_2 (ref. 24) based redox cycles require smaller temperature swings ΔT (*i.e.*, the difference between oxidation and reduction temperature) than all studied perovskites. Compared to CeO_2,[52] ΔT of LSMA6446, the perovskite with the smallest temperature swing, is still about 180 K larger. We note that large temperature swings are undesirable as they introduce additional irreversible heat losses because more sensible heat is needed to heat the redox material from the oxidation temperature to the reduction temperature.

From the investigated perovskites, LSMA6446 shows the most favorable oxidation thermodynamics (*cf.* Fig. 5a). That is, oxidation with CO_2 is favorable at the highest temperature ($T =$ 870 K). In contrast, LSMA2882 exhibits the least favorable oxidation thermodynamics (*cf.* Fig. 5b). As discussed previously,[15,23,24,52,57] higher fuel yields, compared to those obtained with CeO_2, can only be reached with low oxidation temperatures and/or with a large excess of oxidant. Both approaches lead to additional energy penalties due to the required heating of the excess oxidant, the large temperature swings ΔT, and the lower fuel concentrations in the outlet gas requiring additional gas separation. Regarding the reduction, LSMA2882 and LSMA6482 exhibit the most and the least favorable reduction thermodynamics, respectively (*cf.* Fig. 5b).

As a general trend, Fig. 5 shows that the redox thermodynamics of the perovskites with a constant A-cation ratio but varying B-cation ratios (*cf.* Fig. 5a and S8a†) is much less affected in comparison to compositions with varying A-cation ratios and a constant B-cation ratio (*cf.* Fig. 5b and S8a†). The same is observed when Sr is replaced by Ca (*cf.* Fig. S8b†). These results confirm the findings of Deml *et al.*[25] stating that varying the A-cation ratio affects the redox behavior while changing the B-cation ratio does not.

In summary, LSMA6446 shows the most favorable redox characteristics compared to the studied perovskites, owing to its favorable oxidation equilibrium and relatively low ΔT. These desirable redox characteristics can be understood due to relatively high $\Delta\bar{s}^{\circ}_{O}$ values (*cf.* Fig. 4c), leading to a steep slope of $\Delta\bar{g}^{\circ}_{O}$ for $\delta = 0.01$, relative to that of the other perovskites. Furthermore, the reduction of LSMA6446 proceeds at temperatures comparable to those of LSMA6464 and LSMA6482, given the steep decrease of $\Delta\bar{h}^{\circ}_{O}$ with increasing δ (*cf.* Fig. 4a). In contrast, Deml *et al.*[25] used DFT to identify LSMA6464 as an optimal LSMA composition (see above), which we suggest is due to the difference in the assumed operating conditions of the redox cycle.[25]

Electronic structure trends

To understand the experimentally established trends in the redox activity of nonstoichiometric perovskites from an atomic perspective, DFT was employed to predict the thermochemical stability of oxygen vacancies in perovskites. We computed the free energy required to form oxygen vacancies (ΔG_V[O]) at $La_{0.75}Sr_{0.25}Mn_{0.25}Al_{0.75}O_3$ (representing LSMA3113), $La_{0.75}Sr_{0.25}Mn_{0.75}Al_{0.25}O_3$ (LSMA3131), and $La_{0.25}Sr_{0.75}Mn_{0.75}Al_{0.25}O_3$ (LSMA1331) surfaces. These models were chosen to represent compositions with low x_{Sr} and high y_{Al} (LSMA3113), low x_{Sr} and low y_{Al} (LSMA3131), and high x_{Sr} and low y_{Al} (LSMA1331). Making use of correlations between the redox energetics at metal oxide surfaces and those of bulk metal oxides (see the ESI†),[43,44] theoretical Gibbs free energy changes for the reduction and oxidation steps were determined. Fig. 6 compares the measured Gibbs free energy data, $\Delta\bar{g}^{\circ}_{O}$, to the computational data $\Delta\bar{g}^{\circ *}_{O}$, for LSMA1331, LSMA3131 and LSMA3113, shown for $\delta = 0$ (representing oxidation) and $\delta = 0.25$ (representing reduction) from 800 K to 1600 K and from 1200 K to 2000 K, respectively. Solid grey lines represent the right hand side of eqn (15): $\Delta\bar{g}^{\circ}_{O}(\delta, T) = -\frac{1}{2} RT \ln(pO_2/p^{\circ})$ with $pO_2 = 10^{-3}$ bar and dashed grey lines represent the right hand side of eqn (16): $\Delta_r G^{\circ}_{CO_2} = \Delta G^{\circ}_{r} + RT \ln\left(\frac{pCO_2}{pCO}\right)$ for $pCO/pCO_2 = 0.01$.

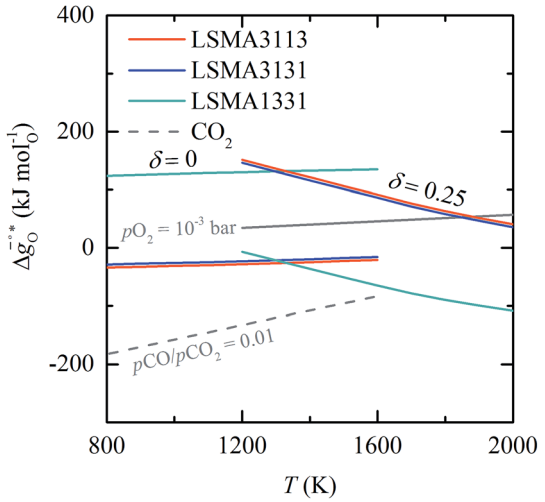

Fig. 6 Standard partial molar Gibbs free energy change $\Delta\bar{g}_O^{\circ *}$ computed *via* DFT as a function of T for LSMA3113, LSMA3131, and LSMA1331 for $\delta = 0.25$ (representing perovskite reduction) and $\delta = 0$, (representing perovskite oxidation). The dashed grey line is the Gibbs free energy change of CO oxidation ($CO + 0.5O_2 = CO_2$), $-\Delta_r G^{\circ}_{CO_2}$ in 1% CO in CO_2 ($pCO/pCO_2 = 0.01$). The perovskite reduction is given at equilibrium in $pO_2 = 10^{-3}$ bar at $\delta = 0.25$ and at temperatures at which eqn (15) holds (grey solid line). The metal oxide oxidation with CO_2 to $\delta = 0$ at $pCO/pCO_2 = 0.01$ is thermodynamically favorable at temperatures where $-\Delta\bar{g}_O^{\circ} = -\Delta_r G^{\circ}_{CO_2}$.

Fig. 6 shows that the DFT-computed energetics follow the redox trends observed experimentally. That is, while the reduction of LSMA1331 is more favorable than the reduction of perovskites with lower x_{Sr}, oxidation of LSMA1331 is thermodynamically less favorable. This is analogous to the trends in the redox energetics of *e.g.* LSMA2882, LSMA6446 and LSMA6464 (*cf.* Fig. 1–3). For these compositions, the reduction extent of LSMA2882 surpasses those of LSMA6446 and LSMA6464. Furthermore, Fig. 6 shows that perovskites with equal A-cation ratios but unequal B-cation ratios (*i.e.*, LSMA3113 and LSMA3131) are characterized by comparable Gibbs free energies, with minor differences of around 5 kJ mol$_O^{-1}$. This is contrasted by the Gibbs free energies of LSMA1331 and LSMA3131, differing by approximately 100 kJ mol$_O^{-1}$, which confirms the experimental trends discussed above. We note that the slight deviation of $\Delta\bar{g}_O^{\circ *}$ as a function of temperature from linearity is likely an artifact of the limited and partly extrapolated thermochemical data (see the ESI†) used to establish the scaling relationships between surface and bulk metal oxide redox energetics.

Conclusions

The investigated perovskites $La_{1-x}Sr_xMn_{1-y}Al_yO_{3-\delta}$ ($0 \le x \le 1$, $0 \le y \le 1$) and $La_{0.6}Ca_{0.4}Mn_{0.8}Al_{0.2}O_{3-\delta}$ showed typically favorable O_2 evolution thermodynamics compared to ceria, which cannot reach equally large oxygen nonstoichiometries under the same process conditions. However, thermodynamically favorable metal oxide reduction resulted consequentially in unfavorable metal oxide oxidation. This redox trade-off translates into increased energy penalties for solar thermochemical splitting of CO_2 and H_2O because of irreversible heat losses due to larger temperature-swing operations compared to CeO_2 and the additional energy requirements for separating the excess CO_2/H_2O oxidant from the CO/H_2 product. On the other hand, lowering the reduction temperatures alleviates thermal and mechanical stress in solar receiver–reactors and decreases volatilization of the redox material. To guide the design of perovskite redox materials, we reported trends in the redox energetics that are particularly sensitive to the A-cation composition. Furthermore, the perovskites show typically decreasing partial molar enthalpy changes for the oxide reduction with increasing oxygen nonstoichiometries. This desirable material characteristic is most pronounced for $La_{0.6}Sr_{0.4}Mn_{0.4}Al_{0.6}O_{3-\delta}$, making it an attractive material for CO_2 and H_2O splitting at relatively moderate process temperatures. The experimentally established energetic trends are confirmed with electronic structure theory computations, such that we suggest a simple DFT-based methodology for estimating the thermodynamic activity of perovskites with variable stoichiometry and valence. While this work focuses on perovskites for solar thermochemical splitting of CO_2, and H_2O, the results are generally relevant for the design of metal oxides for other high-temperature energy conversion applications, such as solid oxide fuel cells, ion transport membranes, and oxygen capacitors.

Nomenclature

$\Delta_r G^{\circ}_{CO_2}$	Standard Gibbs free energy change of CO_2 formation: $CO + 0.5O_2 = CO_2$ (kJ mol$_O^{-1}$)
$\Delta\bar{g}_O^{\circ}$	Standard partial molar Gibbs free energy change of metal oxide reduction (kJ mol$_O^{-1}$)
$\Delta\bar{g}_O^{\circ *}$	Computed standard partial molar Gibbs free energy change of metal oxide reduction (kJ mol$_O^{-1}$)
ΔG_V[O]	Computed Gibbs free energy change of oxygen vacancy formation (eV)
$\Delta\bar{h}_O^{\circ}$	Standard partial molar enthalpy change of metal oxide reduction (kJ mol$_O^{-1}$)
DFT	Density functional theory
K_1	Mn^{4+} to Mn^{3+} defect reaction equilibrium constant (−)
K_2	Mn^{4+} to Mn^{2+} defect reaction equilibrium constant (−)
LCMA6464	$La_{0.6}Ca_{0.4}Mn_{0.6}Al_{0.4}O_3$
LCMA6482	$La_{0.6}Ca_{0.4}Mn_{0.8}Al_{0.2}O_3$
LSMA1331	$La_{0.25}Sr_{0.75}Mn_{0.75}Al_{0.25}O_3$
LSMA3113	$La_{0.75}Sr_{0.25}Mn_{0.25}Al_{0.75}O_3$
LSMA3131	$La_{0.75}Sr_{0.25}Mn_{0.75}Al_{0.25}O_3$
LSMA2882	$La_{0.2}Sr_{0.8}Mn_{0.8}Al_{0.2}O_3$
LSMA4664	$La_{0.4}Sr_{0.6}Mn_{0.6}Al_{0.4}O_3$
LSMA4682	$La_{0.4}Sr_{0.6}Mn_{0.8}Al_{0.2}O_3$
LSMA6464	$La_{0.6}Sr_{0.4}Mn_{0.6}Al_{0.4}O_3$
LSMA6482	$La_{0.6}Sr_{0.4}Mn_{0.8}Al_{0.2}O_3$
M_O	Molar mass of O (g mol^{-1})
M_s	Molar mass of reactive sample (g mol^{-1})
m_s	Mass of reactive sample (mg)

Δm_s	Relative mass of reactive sample (−)
mL min^{-1}	Standard liter per minute at 298 K and 1 bar
pO_2	Oxygen partial pressure (mbar)
p_{tot}	System pressure (bar)
p°	Standard pressure (bar)
R	Universal gas constant (J mol_O^{-1} K^{-1})
$\Delta\bar{s}_O^\circ$	Standard partial molar entropy change of metal oxide reduction (J mol_O^{-1} K^{-1})
T	Temperature (K)
TGA	Thermogravimetric analyzer
ΔT	Difference between oxidation and reduction temperatures (K)
x	A-Site molar dopant concentration (−)
XRD	X-ray diffraction
y	B-Site molar dopant concentration (−)
δ	Degree of oxygen nonstoichiometry at thermodynamic equilibrium (−)
δ_{ox}	Degree of oxygen nonstoichiometry after oxidation at thermodynamic equilibrium (−)
δ_{red}	Degree of oxygen nonstoichiometry after reduction at thermodynamic equilibrium (−)

Acknowledgements

We gratefully acknowledge the financial support from the Swiss National Science Foundation (No. 200021-162435), the Helmholtz-Gemeinschaft Deutscher Forschungszentren (Virtuelles Institut SolarSyngas), and the European Research Council under the European Union's ERC Advanced Grant (SUNFUELS-No. 320541). The DFT calculations were performed at the High-Performance Computation cluster of ETH Zürich.

References

1 W. C. Chueh, C. Falter, M. Abbott, D. Scipio, P. Furler, S. M. Haile and A. Steinfeld, *Science*, 2010, **330**, 1797–1801.
2 M. Romero and A. Steinfeld, *Energy Environ. Sci.*, 2012, **5**, 9234–9245.
3 C. K. Yang, Y. Yamazaki, A. Aydin and S. M. Haile, *J. Mater. Chem. A*, 2014, **2**, 13612–13623.
4 J. S. Luo, J. H. Im, M. T. Mayer, M. Schreier, M. K. Nazeeruddin, N. G. Park, S. D. Tilley, H. J. Fan and M. Grätzel, *Science*, 2014, **345**, 1593–1596.
5 A. Steinfeld, P. Kuhn, A. Reller, R. Palumbo, J. Murray and Y. Tamaura, *Int. J. Hydrogen Energy*, 1998, **23**, 767–774.
6 L. M. Utschig, S. C. Silver, K. L. Mulfort and D. M. Tiede, *J. Am. Chem. Soc.*, 2011, **133**, 16334–16337.
7 W. Zhu, Y.-J. Zhang, H. Zhang, H. Lv, Q. Li, R. Michalsky, A. A. Peterson and S. Sun, *J. Am. Chem. Soc.*, 2014, **136**, 16132–16135.
8 D. Marxer, P. Furler, J. Scheffe, H. Geerlings, C. Falter, V. Batteiger, A. Sizmann and A. Steinfeld, *Energy Fuels*, 2015, **29**, 3241–3250.
9 J. R. Scheffe and A. Steinfeld, *Mater. Today*, 2014, **17**, 341–348.
10 W. C. Chueh and S. M. Haile, *ChemSusChem*, 2009, **2**, 735–739.
11 W. C. Chueh and S. M. Haile, *Philos. Trans. R. Soc., A*, 2010, **368**, 3269–3294.
12 E. A. Fletcher, *J. Sol. Energy Eng.*, 2001, **123**, 63–74.
13 M. Roeb, M. Neises, N. Monnerie, F. Call, H. Simon, C. Sattler, M. Schmucker and R. Pitz-Paal, *Materials*, 2012, **5**, 2015–2054.
14 P. Furler, J. Scheffe, M. Gorbar, L. Moes, U. Vogt and A. Steinfeld, *Energy Fuels*, 2012, **26**, 7051–7059.
15 J. R. Scheffe, D. Weibel and A. Steinfeld, *Energy Fuels*, 2013, **27**, 4250–4257.
16 R. Bader, L. J. Venstrom, J. H. Davidson and W. Lipinski, *Energy Fuels*, 2013, **27**, 5533–5544.
17 S. Ackermann, L. Sauvin, R. Castiglioni, J. L. M. Rupp, J. R. Scheffe and A. Steinfeld, *J. Phys. Chem. C*, 2015, **119**, 16452–16461.
18 N. Knoblauch, L. Dörrer, P. Fielitz, M. Schmücker and G. Borchardt, *Phys. Chem. Chem. Phys.*, 2015, **17**, 5849–5860.
19 A. H. McDaniel, E. C. Miller, D. Arifin, A. Ambrosini, E. N. Coker, R. O'Hayre, W. C. Chueh and J. H. Tong, *Energy Environ. Sci.*, 2013, **6**, 2424–2428.
20 A. Demont, S. Abanades and E. Beche, *J. Phys. Chem. C*, 2014, **118**, 12682–12692.
21 S. Dey, B. S. Naidu, A. Govindaraj and C. N. R. Rao, *Phys. Chem. Chem. Phys.*, 2015, **17**, 122–125.
22 A. Demont and S. Abanades, *J. Mater. Chem. A*, 2015, **3**, 3536–3546.
23 T. Cooper, J. R. Scheffe, M. E. Galvez, R. Jacot, G. Patzke and A. Steinfeld, *Energy Technol.*, 2015, **3**, 1130–1142.
24 M. Takacs, M. Hoes, M. Caduff, T. Cooper, J. R. Scheffe and A. Steinfeld, *Acta Mater.*, 2016, 700–710.
25 A. M. Deml, V. Stevanovic, A. M. Holder, M. Sanders, R. O'Hayre and C. B. Musgrave, *Chem. Mater.*, 2014, **26**, 6595–6602.
26 S. Dey, B. S. Naidu and C. N. R. Rao, *Chem.–Eur. J.*, 2015, **21**, 7077–7081.
27 A. H. Bork, M. Kubicek, M. Struzik and J. L. M. Rupp, *J. Mater. Chem. A*, 2015, **3**, 15546–15557.
28 J. H. Kuo, H. U. Anderson and D. M. Sparlin, *J. Solid State Chem.*, 1989, **83**, 52–60.
29 F. A. Kröger and H. J. Vink, *Solid State Phys.*, 1956, **3**, 307–435.
30 J. A. M. Van Roosmalen and E. H. P. Cordfunke, *J. Solid State Chem.*, 1991, **93**, 212–219.
31 J. A. M. Van Roosmalen and E. H. P. Cordfunke, *J. Solid State Chem.*, 1994, **110**, 113–117.
32 J. Nowotny and M. Rekas, *J. Am. Ceram. Soc.*, 1998, **81**, 67–80.
33 J. Mizusaki, N. Mori, H. Takai, Y. Yonemura, H. Minamiue, H. Tagawa, M. Dokiya, H. Inaba, K. Naraya, T. Sasamoto and T. Hashimoto, *Solid State Ionics*, 2000, **129**, 163–177.
34 M. Oishi, K. Yashiro, K. Sato, J. Mizusaki and T. Kawada, *J. Solid State Chem.*, 2008, **181**, 3177–3184.
35 S. Sengodan, J. Kim, J. Shin and G. Kim, *J. Electrochem. Soc.*, 2011, **158**, B1373–B1379.
36 A. Y. Zuev and D. S. Tsvetkov, *Solid State Ionics*, 2010, **181**, 557–563.
37 J. Enkovaara, C. Rostgaard, J. J. Mortensen, J. Chen, M. Dulak, L. Ferrighi, J. Gavnholt, C. Glinsvad, V. Haikola,

H. A. Hansen, H. H. Kristoffersen, M. Kuisma, A. H. Larsen, L. Lehtovaara, M. Ljungberg, O. Lopez-Acevedo, P. G. Moses, J. Ojanen, T. Olsen, V. Petzold, N. A. Romero, J. Stausholm-Moller, M. Strange, G. A. Tritsaris, M. Vanin, M. Walter, B. Hammer, H. Hakkinen, G. K. H. Madsen, R. M. Nieminen, J. Nørskov, M. Puska, T. T. Rantala, J. Schiotz, K. S. Thygesen and K. W. Jacobsen, *J. Phys.: Condens. Matter*, 2010, **22**, 253202.

38 J. J. Mortensen, L. B. Hansen and K. W. Jacobsen, *Phys. Rev. B: Condens. Matter Mater. Phys.*, 2005, **71**, 035109.

39 S. R. Bahn and K. W. Jacobsen, *Comput. Sci. Eng.*, 2002, **4**, 56–66.

40 B. Hammer, L. B. Hansen and J. K. Nørskov, *Phys. Rev. B: Condens. Matter Mater. Phys.*, 1999, **59**, 7413–7421.

41 A. J. Medford, J. Wellendorff, A. Vojvodic, F. Studt, F. Abild-Pedersen, K. W. Jacobsen, T. Bligaard and J. K. Norskov, *Science*, 2014, **345**, 197–200.

42 M. García-Mota, A. Vojvodic, H. Metiu, I. C. Man, H. Y. Su, J. Rossmeisl and J. K. Nørskov, *ChemCatChem*, 2011, **3**, 1607–1611.

43 M. Ezbiri, K. M. Allen, M. E. Gàlvez, R. Michalsky and A. Steinfeld, *ChemSusChem*, 2015, **8**, 1966–1971.

44 R. Michalsky, V. Botu, C. M. Hargus, A. A. Peterson and A. Steinfeld, *Adv. Energy Mater.*, 2014, **4**, 1401082.

45 I. Barin, *Thermochemical Data of Pure Substances*, 1993.

46 A. M. Glazer, *Acta Crystallogr.*, 1975, **31**, 756–762.

47 M. A. Peña and J. L. G. Fierro, *Chem. Rev.*, 2001, **101**, 1981–2017.

48 M. E. Gálvez, R. Jacot, J. Scheffe, T. Cooper, G. Patzke and A. Steinfeld, *Phys. Chem. Chem. Phys.*, 2015, **17**, 6629–6634.

49 S. M. Babiniec, E. N. Coker, J. E. Miller and A. Ambrosini, *Sol. Energy*, 2015, **118**, 451–459.

50 H. Lehnert, H. Boysen, J. Schneider, F. Frey, D. Hohlwein, P. Radaelli and H. Ehrenberg, *Z. Kristallogr.*, 2000, **215**, 536–541.

51 P. M. Woodward, T. Vogt, D. E. Cox, A. Arulraj, C. N. R. Rao, P. Karen and A. K. Cheetham, *Chem. Mater.*, 1998, **10**, 3652–3665.

52 M. Takacs, J. R. Scheffe and A. Steinfeld, *Phys. Chem. Chem. Phys.*, 2015, **17**, 7813–7822.

53 A. Demont and S. Abanades, *RSC Adv.*, 2014, **4**, 54885–54891.

54 Y. L. Lee, J. Kleis, J. Rossmeisl, Y. Shao-Horn and D. Morgan, *Energy Environ. Sci.*, 2011, **4**, 3966–3970.

55 A. Grimaud, K. J. May, C. E. Carlton, Y. L. Lee, M. Risch, W. T. Hong, J. G. Zhou and Y. Shao-Horn, *Nat. Commun.*, 2013, **4**, 2439.

56 W. G. Mallard and P. J. Linstrom, *NIST Chemistry WebBook, NIST Standard Reference Database Number 69*, National Institute of Standards and Technology, Gaithersburg MD, 1998, http://webbook.nist.gov.

57 J. R. Scheffe and A. Steinfeld, *Energy Fuels*, 2012, **26**, 1928–1936.